



# Pushing the conductance and transparency limit of monolayer graphene electrodes for flexible organic light-emitting diodes

Lai-Peng Ma<sup>a,b</sup>, Zhongbin Wu<sup>c</sup>, Lichang Yin<sup>a,b</sup>, Dingdong Zhang<sup>a,b</sup>, Shichao Dong<sup>a,b</sup>, Qing Zhang<sup>a,b</sup>, Mao-Lin Chen<sup>a,b</sup>, Wei Ma<sup>a,b</sup>, Zhibin Zhang<sup>d</sup>, Jinhong Du<sup>a,b</sup>, Dong-Ming Sun<sup>a,b</sup>, Kaihui Liu<sup>d</sup>, Xiangfeng Duan<sup>e</sup>, Dongge Ma<sup>f</sup>, Hui-Ming Cheng<sup>a,b,g</sup>, and Wencai Ren<sup>a,b,1</sup>

<sup>a</sup>Shenyang National Laboratory for Materials Science, Institute of Metal Research, Chinese Academy of Sciences, 110016 Shenyang, China; <sup>b</sup>School of Materials Science and Engineering, University of Science and Technology of China, 110016 Shenyang, China; <sup>c</sup>State Key Laboratory of Polymers Physics and Chemistry, Changchun Institute of Applied Chemistry, Chinese Academy of Sciences, 130022 Changchun, China; <sup>d</sup>State Key Laboratory for Mesoscopic Physics, School of Physics, Peking University, 100871 Beijing, China; <sup>e</sup>Department of Chemistry and Biochemistry, University of California, Los Angeles, CA 90095; <sup>f</sup>State Key Laboratory of Luminescent Materials & Devices, South China University of Technology, 510640 Guangzhou, China; and <sup>g</sup>Shenzhen Geim Graphene Center, Tsinghua-Berkeley Shenzhen Institute, Tsinghua University, 518055 Shenzhen, China

Edited by Andrea C. Ferrari, University of Cambridge, Cambridge, United Kingdom, and accepted by Editorial Board Member Angel Rubio August 31, 2020 (received for review December 22, 2019)

Graphene has emerged as an attractive candidate for flexible transparent electrode (FTE) for a new generation of flexible optoelectronics. Despite tremendous potential and broad earlier interest, the promise of graphene FTE has been plagued by the intrinsic trade-off between electrical conductance and transparency with a figure of merit ( $\sigma_{DC}/\sigma_{OP}$ ) considerably lower than that of the state-of-the-art ITO electrodes ( $\sigma_{DC}/\sigma_{OP} < 123$  for graphene vs.  $\sim 240$  for ITO). Here we report a synergistic electrical/optical modulation strategy to simultaneously boost the conductance and transparency. We show that a tetrakis(pentafluorophenyl)boric acid (HTB) coating can function as highly effective hole doping layer to increase the conductance of monolayer graphene by sevenfold and at the same time as an anti-reflective layer to boost the visible transmittance to 98.8%. Such simultaneous improvement in conductance and transparency breaks previous limit in graphene FTEs and yields an unprecedented figure of merit ( $\sigma_{DC}/\sigma_{OP} \sim 323$ ) that rivals the best commercial ITO electrode. Using the tailored monolayer graphene as the flexible anode, we further demonstrate high-performance green organic light-emitting diodes (OLEDs) with the maximum current, power and external quantum efficiencies ( $111.4 \text{ cd A}^{-1}$ ,  $124.9 \text{ lm W}^{-1}$  and 29.7%) outperforming all comparable flexible OLEDs and surpassing that with standard rigid ITO by 43%. This study defines a straightforward pathway to tailor optoelectronic properties of monolayer graphene and to fully capture their potential as a generational FTE for flexible optoelectronics.

flexible optoelectronics | graphene | transparent electrode | doping | antireflection

Flexible transparent electrode (FTE) is one of the most promising applications of graphene due to its excellent flexibility, superior broadband transmittance, good electrical conductivity, atomically smooth surface, high chemical/thermal stability and widely tunable work function. It shows distinct advantage over the predominant tin-doped indium oxide (ITO) electrode, which suffers from intrinsic brittleness, increasingly high cost and detrimental ion diffusion. However, it remains a significant challenge to develop high-performance graphene FTEs that rival the state-of-the-art ITO films in terms of the figure of merit (FoM, direct current conductivity to optical conductivity ratio:  $\sigma_{DC}/\sigma_{OP}$ ) (1, 2). The performance of graphene transparent electrodes has been generally plagued by the intrinsic trade-off between electrical conductance and transparency as described by the Beer–Lambert law (3). This dilemma is obvious for the physical strategies such as multilayer stacking, hybridizing, and fabricating a holey structure, in which the improvement of one property leads to significant degradation of the other because the two are inversely affected by

the geometry of film (4–7). The distinctive linear dispersion relation of graphene allows improvement in both electrical and optical properties by tuning the Fermi level with doping (2). The widely used surface charge transfer (SCT) dopants effectively improve the electrical conductivity by increasing the carrier concentration of graphene over one order of magnitude, but they invariably cause transparency reduction (e.g.,  $\sim 2\%$  for the strong p-dopants  $\text{AuCl}_3$  and  $\text{HNO}_3$ ) instead of enhancement. They also suffer from severe performance degradation over time and heating (8). Although lithium intercalation doping enables simultaneous improvement in conductivity and transparency of few-layer graphene under inert atmosphere by suppressing the interband transition, the enhancements vanish within several hours upon exposure to ambient conditions because lithium intercalation is extremely sensitive to moisture (9). Therefore, breaking the dilemma between electrical conductance and optical transmittance of graphene requires new modulation strategies and mechanisms.

## Significance

Although graphene shows great promise as a generational flexible transparent electrode (FTE), its development has been severely limited by the intrinsic trade-off between electrical conductance and transparency with the performance metrics inferior to that of the state-of-the-art ITO electrodes. We report a straightforward approach to break previous limit in graphene FTEs and yield an unprecedented performance that rivals the best commercial ITO electrode. Using the tailored monolayer graphene FTE, we further demonstrate high-performance flexible green organic light-emitting diodes (OLEDs) with the efficiencies outperforming all comparable flexible OLEDs and surpassing that with rigid ITO anode. This simple strategy will boost the development of next-generation flexible optoelectronics beyond the dominant rigid platforms.

Author contributions: L.-P.M. and W.R. designed research; L.-P.M., Z.W., L.Y., D.Z., S.D., Q.Z., M.-L.C., and W.M. performed research; Z.Z. and K.L. contributed new reagents/analytic tools; L.-P.M., Z.W., L.Y., D.Z., M.-L.C., J.D., D.-M.S., D.M., and W.R. analyzed data; and L.-P.M., L.Y., X.D., H.-M.C., and W.R. wrote the paper.

The authors declare no competing interest.

This article is a PNAS Direct Submission. A.C.F. is a guest editor invited by the Editorial Board.

This open access article is distributed under Creative Commons Attribution-NonCommercial-NoDerivatives License 4.0 (CC BY-NC-ND).

<sup>1</sup>To whom correspondence may be addressed. Email: wcren@imr.ac.cn.

This article contains supporting information online at <https://www.pnas.org/lookup/suppl/doi:10.1073/pnas.1922521117/-DCSupplemental>.

First published October 5, 2020.

Here, we propose a synergistic electrical/optical modulation strategy to simultaneously boost the conductance and transparency of graphene FTE. We show that a tetrakis(pentafluorophenyl)boric acid  $[[\text{H}(\text{OEt})_2]_2]^+[\text{B}(\text{C}_6\text{F}_5)_4]^-$  or HTB coating, a unique proton donor with low refractive index, can function as a highly effective hole-doping layer to increase the electrical conductance of monolayer graphene by sevenfold and at the same time as an antireflective layer to boost the visible transmittance to 98.8%. Such simultaneous improvement in conductance and transparency breaks previous limit in graphene FTEs and yields an unprecedented FoM ( $\sigma_{\text{DC}}/\sigma_{\text{Op}} \sim 323$ ) that rivals the best commercial ITO electrode. Using the tailored monolayer graphene as the flexible anode, we further demonstrate high-performance green organic light-emitting diodes (OLEDs) with the maximum efficiencies outperforming all comparable flexible OLEDs and surpassing that with standard rigid ITO anode.

## Results and Discussion

**Simultaneous Improvement in Electrical Conductance and Optical Transmittance.** HTB is an organic protic acid with the structure as shown in Fig. 1A, which is highly soluble in various common solvents such as water, ethanol, acetone, and nitromethane (10). We prepared the HTB coating on graphene simply by dipping flexible graphene/polyethylene terephthalate (PET) film in the nitromethane solution of HTB at room temperature for several minutes, followed by nitrogen flow drying. This coating process is easy to scale up, without limitation on the size of graphene and processing temperature/atmosphere. Because of the unavoidable nonuniformity of Cu foil substrate, the chemical vapor deposition (CVD)-grown large-area monolayer graphene films are usually decorated with numerous small graphene islands and predominantly show an optical transmittance around 97% (SI Appendix, Fig. S1). In our study, we chose such representative graphene films as raw material to show the effect of HTB coating.

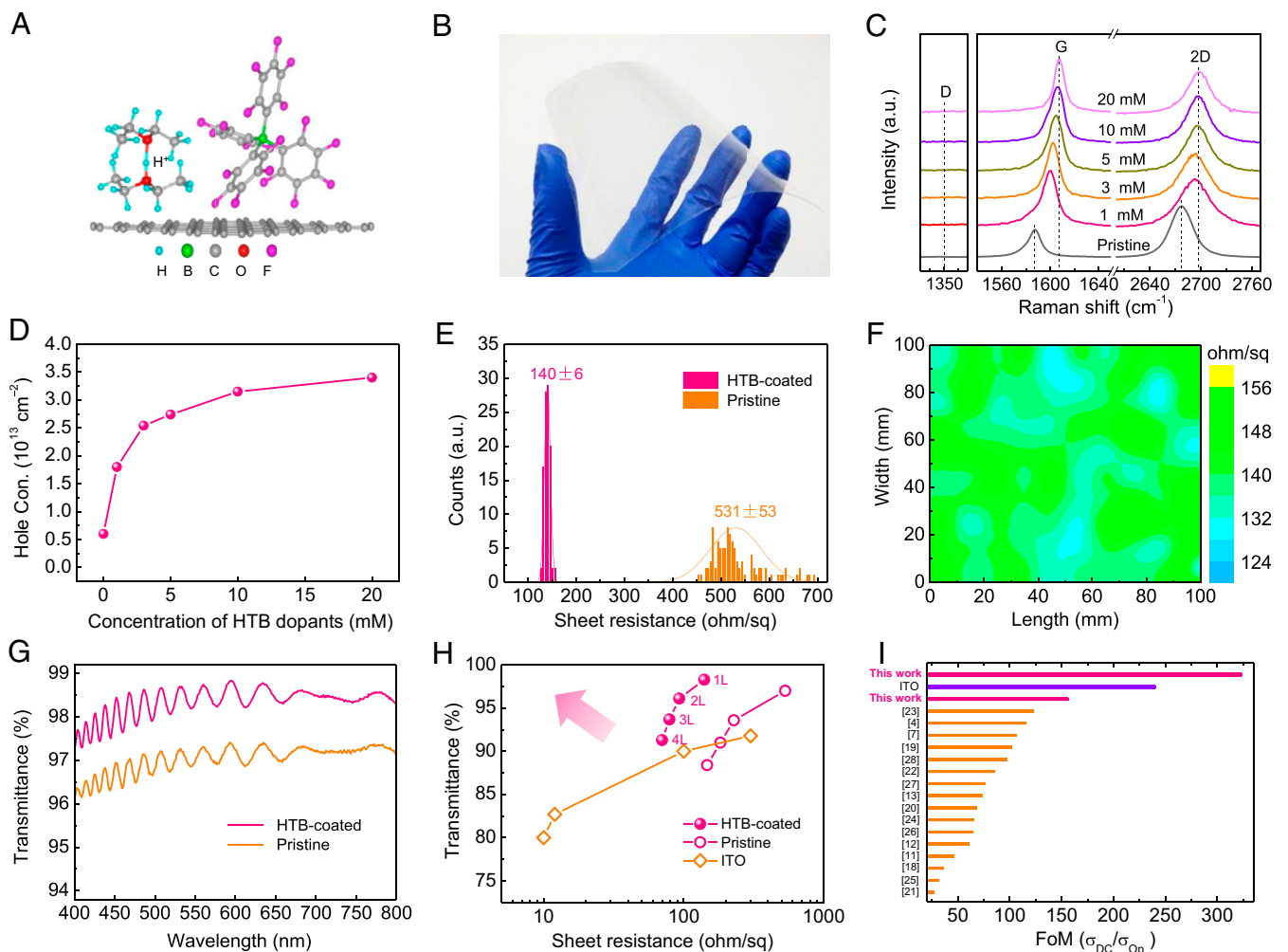


**Fig. 1.** Simultaneous improvement in electrical conductance and optical transmittance of graphene enabled by the HTB coating. (A) Schematic chemical structure of HTB on graphene. A typical HTB molecule consists of a proton coordinated with two ether molecules and a tetrakis(pentafluorophenyl)borate anion. (B) Photograph of a large-area flexible HTB-coated monolayer graphene/PET film ( $10 \times 10 \text{ cm}^2$ ). (C) Raman spectra of monolayer graphene coated with different concentrations of HTB. (D) Hole concentration of HTB-coated monolayer graphene as a function of HTB concentration. (E) Sheet resistance distribution of a  $10 \times 10 \text{ cm}^2$  monolayer graphene/PET film before and after coating with 20 mM HTB. (F) Sheet resistance mapping of the HTB-coated monolayer graphene/PET film. (G) Optical transmittance spectra of monolayer graphene/PET film before and after coating with 20 mM HTB (excluding the PET substrate). (H) Sheet resistance versus optical transmittance ( $\lambda = 550 \text{ nm}$ ) of graphene/PET film (1–4-layer graphene) before and after coating with 20 mM HTB. The performances of state-of-the-art ITO films are included as reference (2). (I) Optoelectronic performance comparison ( $\sigma_{\text{DC}}/\sigma_{\text{Op}}$ ) of HTB-coated graphene FTEs with representative doped graphene FTEs and ITO (2).

Fig. 1B shows an HTB-coated highly transparent graphene/PET film with a size of  $10 \times 10 \text{ cm}^2$ . We first used Raman spectroscopy to study the effect of HTB coating on the electrical properties and structure of graphene. As the concentration of HTB increases, both Raman G and 2D peaks of the HTB-coated monolayer graphene continuously blueshift together with a decrease in  $I_{2D}/I_G$  ratio (Fig. 1C and *SI Appendix*, Fig. S2), suggesting that graphene is p-doped by HTB. Notably, the G peak blueshifts by  $20 \text{ cm}^{-1}$  from  $1,587$  to  $1,607 \text{ cm}^{-1}$  with  $20 \text{ mM}$  HTB doping, which is comparable to the effect of strong p-dopants for graphene (11–14). The absence of D peaks indicates that graphene retains its original high quality with the HTB coating, which is physisorbed without forming defects or  $\text{sp}^3$  structure in graphene. Further analysis of the frequencies of G and 2D peaks confirms the dominant p-doping effect in HTB-doped graphene (*SI Appendix*, Fig. S2C) (15). Moreover, it reveals that the pristine graphene is under tensile strain, which is converted into small compressive strain upon coating with HTB. A close inspection of 2D peak indicates that its full width at half maximum (FWHM) increases from  $32$  to  $46 \text{ cm}^{-1}$  with  $1 \text{ mM}$  HTB, followed by a gradual decrease to  $34 \text{ cm}^{-1}$  with further increasing HTB concentration to  $20 \text{ mM}$ , as shown in *SI Appendix*, Fig. S2D. The evolution of the FWHM of 2D peak is related to the strain variation in the plane of graphene (16), which might be due to the morphology change of HTB coating from islands to a continuous film with increasing HTB concentration, as shown in *SI Appendix*, Fig. S3.

We then quantitatively evaluated the doping strength by using Hall measurements. As shown in Fig. 1D, the pristine graphene shows a moderate p-doping feature with a carrier concentration of  $6.1 \times 10^{12} \text{ cm}^{-2}$ . Consistent with the evolution of Raman spectra, the HTB coating allows a rapid increase in the carrier concentration below  $5 \text{ mM}$  followed by a slow increase until  $20 \text{ mM}$ . The  $20\text{-mM}$  treatment yields a nearly sixfold improvement in hole concentration to  $3.4 \times 10^{13} \text{ cm}^{-2}$ . The strong p-doping effect of HTB coating significantly improves the electrical conductance of graphene. The monolayer sample coated with  $20 \text{ mM}$  HTB shows a large drop of  $74\%$  in sheet resistance ( $R_s$ ) from  $531 \pm 53 \text{ }\Omega/\square$  to  $140 \pm 6 \text{ }\Omega/\square$  (Fig. 1E). Such large enhancements of hole concentration and electrical conductivity are even comparable to the effect of heavy doping with  $\text{AuCl}_3$ , the strongest SCT dopants for graphene reported so far (8). In addition, the HTB doping greatly improves the uniformity of  $R_s$  distribution, with largely reduced SD ( $\pm 6 \text{ }\Omega/\square$ ) as compared to the pristine film ( $\pm 53 \text{ }\Omega/\square$ ) over a large area of  $10 \times 10 \text{ cm}^2$  (Fig. 1E and F). We also investigated the mechanical flexibility of monolayer graphene film coated with  $20 \text{ mM}$  HTB by examining its resistance change under tensile strain. As shown in *SI Appendix*, Fig. S4, the HTB-coated graphene film withstands up to  $6\%$  tensile strain with a small resistance increase of  $5.6\%$ , which is comparable to the pristine graphene ( $3.6\%$ ). These results demonstrate the high mechanical flexibility of HTB-coated graphene.

More importantly, in sharp contrast to the inevitable transparency loss caused by typical p-dopants, the HTB coating simultaneously improves the transparency of graphene/PET films over the entire visible range (Fig. 1G). Consistent with the change of conductance, the optical transmittance increases over the concentration of HTB (*SI Appendix*, Figs. S5A and S6A). Monolayer graphene coated with  $20 \text{ mM}$  HTB shows a high transparency of  $98.3\%$  at  $\lambda = 550 \text{ nm}$ ,  $1.3\%$  increase in absolute value compared to the pristine monolayer graphene used ( $97\%$ ). The optical images provide direct evidence of the substantial increase in transparency caused by the HTB coating (*SI Appendix*, Fig. S5B). This favorable effect of HTB coating is also observed in few-layer graphene films. Fig. 1H clearly reveals that HTB coating enables simultaneous improvement in conductance and transparency of mono- and few-layer graphene FTEs, thus showing a desirable shift toward the top

left corner in the transmittance vs. sheet resistance plot with significantly improved FoM up to  $156$  (Fig. 1I). They demonstrate distinct advantage over state-of-the-art ITO electrodes in the high-transmittance region ( $\geq 90\%$ ).

Such simultaneous improvement was further demonstrated by using the sample close to the perfect structure, CVD-grown single-crystal monolayer graphene (*SI Appendix*, Fig. S6B). Interestingly, the single-crystal film coated with  $20 \text{ mM}$  HTB shows an even larger drop of  $85\%$  in  $R_s$  from  $657 \pm 39 \text{ }\Omega/\square$  to  $96 \pm 4 \text{ }\Omega/\square$  (or  $6.8\text{-fold}$  increase in conductance) together with a  $1.3\%$  absolute increase in visible transparency ( $\lambda = 550 \text{ nm}$ ) from  $97.5$  to  $98.8\%$ , yielding a dramatically enhanced FoM of  $323$  (Fig. 1I). According to the classical theory, the conductance is positively proportional to the product of carrier concentration and mobility. As shown in *SI Appendix*, Table S1, for the pristine samples, single-crystal graphene shows a larger carrier mobility but a much smaller carrier concentration than the polycrystalline film. This is presumably due to the weaker unintentional doping of single-crystal graphene in the absence of grain boundaries that act as preferential sites for charge-transfer adsorbates. Consequently, the pristine single-crystal graphene shows a higher  $R_s$ . After doping with  $20 \text{ mM}$  HTB, a continuous film was formed on the surface of graphene (*SI Appendix*, Fig. S3). In this case, the adsorbed dopants on the grain boundaries only make a small contribution to carrier concentration. As a result, single-crystal and polycrystalline graphene samples show comparable carrier concentrations. However, the presence of doping adsorbates at grain boundaries causes significant reduction in the carrier mobility of polycrystalline graphene due to the strong charge scattering effects (17). Therefore, single-crystal graphene shows larger electrical improvement than polycrystalline graphene after doping. The above results also suggest that HTB coating is a highly effective and versatile strategy for simultaneously improving the conductance and visible transparency of graphene. Note that the FoM of our HTB-coated graphene outperforms all of the doped flexible graphene FTEs (4, 7, 11, 12, 13, 14, 18–28), with a  $>263\%$  improvement, and even rivals the best commercial ITO/glass (FoM:  $120 - 240$ ) (2).

**Excellent Doping Stability and Work Function Modulation.** Equally important, HTB-coated graphene films show excellent ambient stability in both electrical and optical performances, which is crucial for realistic device applications. We evaluated the electrical performance stability by monitoring the change of carrier concentration and  $R_s$  under ambient condition. For comparison, four typical p-dopants ( $\text{AuCl}_3$ ,  $\text{HNO}_3$ , OA, and TFSA) were also studied. After 2 mo, the hole concentration of HTB-coated graphene slightly decreases by  $12\%$  while the samples doped by  $\text{AuCl}_3$ ,  $\text{HNO}_3$ , OA, and TFSA show large degradation of  $37$ ,  $38$ ,  $53$ , and  $29\%$ , respectively (Fig. 2A and C). As a result, the  $R_s$  of HTB-coated sample shows higher long-term ambient stability with a small increase of  $14\%$  after 2 mo (Fig. 2B and C). In contrast, the  $R_s$  of other samples increases by  $1.3\text{--}2.2$  times. Meanwhile, the high transmittances of HTB-coated samples are well retained (Fig. 2D and *SI Appendix*, Fig. S7). Such high ambient stability of HTB-coated graphene film is superior to that of Li-intercalated ultrathin graphite, whose conductance and optical transmittance can be simultaneously improved but vanish within several hours upon exposure to air (9).

Thermally stable transparent electrodes are desired for device fabrication that involves postannealing. We further investigated the  $R_s$  and transparency variation of HTB-coated graphene films over time at  $100 \text{ }^\circ\text{C}$ . As shown in *SI Appendix*, Fig. S8,  $R_s$  shows a small increase of  $4\%$  while the transparency decreases to  $97.7\%$  after annealing at  $100 \text{ }^\circ\text{C}$  for  $60 \text{ min}$ . This result indicates that HTB is prone to thermal treatment, which is a common issue for small-molecule dopants (8). More efforts are needed to improve the thermal stability of HTB doping in future work, in which the

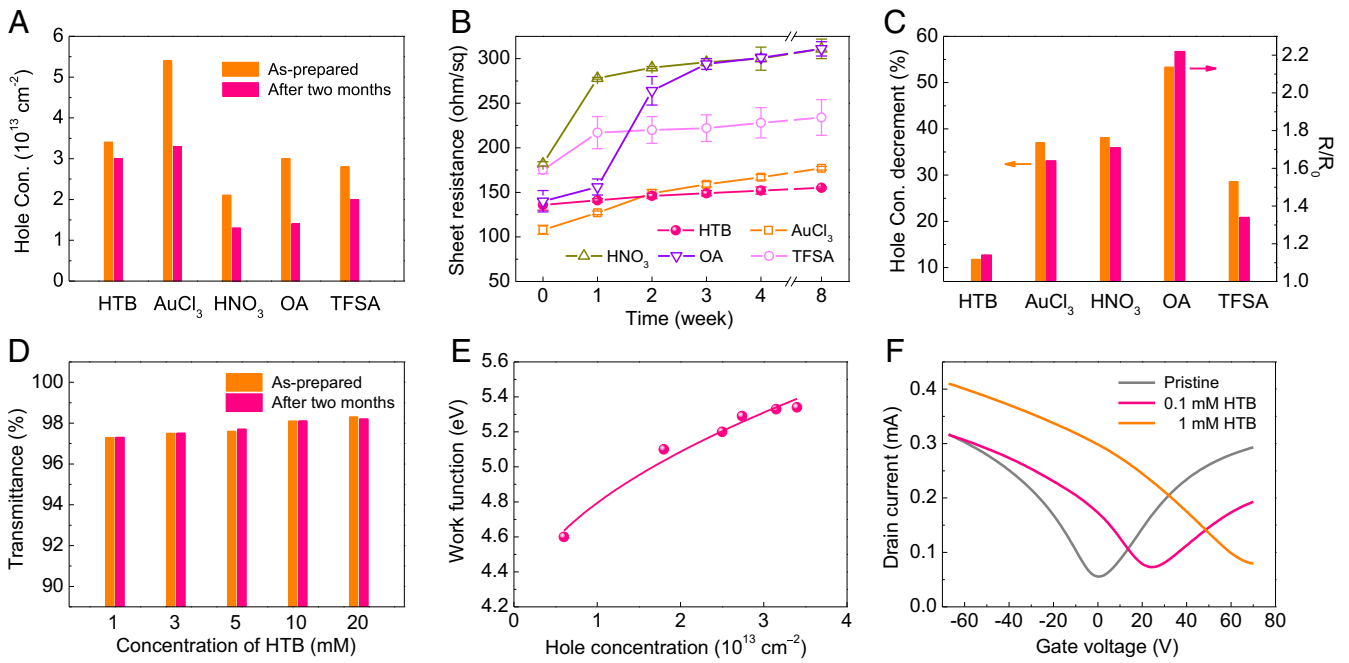


**Fig. 2.** Doping stability and work-function modulation. (A) Hole concentration of the graphene films coated with HTB and doped with different dopants before and after ambient storage for 2 mo. (B) Sheet resistance of the graphene films coated with HTB and doped with different dopants as a function of ambient storage time. The error bars represent the 5D of sheet resistances. (C) Variation in hole concentration and sheet resistance of graphene films coated with HTB and doped with different dopants after ambient storage for 2 mo. The concentrations of HTB and all dopants are 20 mM. (D) Optical transmittance ( $\lambda = 550$  nm) of graphene FTEs coated with different concentrations of HTB before and after ambient storage for 2 mo. (E) Work function of the HTB-coated graphene films as a function of hole concentration. The curve is obtained by fitting the data with the function of  $E_f = h\nu_f(\pi n)^{0.5}$  (32). (F) Transfer characteristics of FETs fabricated by using graphene doped with different concentrations of HTB. Low concentrations were used because high-concentration doping shifts  $V_{\text{Dirac}}$  far beyond the measurement scope of devices.

synthesis of polymeric HTB might be a promising solution, similar to the stable doping of macromolecular acid (29).

Hole doping with HTB also significantly improves the work function of graphene, which is crucial for its use as electrodes to boost the hole injection/extraction in OLEDs, solar cells, and organic field-effect transistors (FETs) with improved energy level alignment. Ultraviolet photoelectron spectroscopy (UPS) spectra show that the work function of graphene increases by 0.7 eV from 4.6 to 5.3 eV as the concentration of HTB increases from 0 to 5 mM and then remains almost unchanged with further increasing the concentration until 20 mM (SI Appendix, Fig. S9A). Note that the work function (5.3 eV) achieved at  $\geq 5$  mM HTB doping is higher than that of ozone-treated ITO electrode ( $\sim 5.1$  eV) (11) and comparable to that of graphene with strong p-doping (4, 11, 14, 21, 25, 30, 31). Quantitative analysis reveals that the evolution of work function generally follows a power-function relation with the hole concentration of graphene (Fig. 2E), as determined by the graphene linear band structure (32). This result clearly shows that the Fermi level of graphene can be effectively downshifted by the strong hole doping with HTB. This effect is further confirmed by the modulation of Dirac voltage ( $V_{\text{Dirac}}$ ) of graphene FET. As shown in Fig. 2F,  $V_{\text{Dirac}}$  is shifted from  $\sim 0$  to  $+23$  V even by using an extremely low HTB concentration of 0.1 mM, and beyond  $+70$  V with 1-mM doping. For the latter, hole concentration is estimated to be larger than  $1 \times 10^{13} \text{ cm}^{-2}$  by using the equation  $n = \alpha V_{\text{Dirac}}$  ( $\alpha = 2.2 \times 10^{11} \text{ cm}^{-2} \cdot \text{V}^{-1}$  for 100-nm-thick  $\text{SiO}_2$ ) (33). This value corresponds to an  $\sim 0.4$  eV Fermi level shift ( $E_f$ ) for the 1-mM sample, which agrees with the work-function increment measured by UPS (32). The work-function saturation at higher concentration of HTB suggests the contribution of other mechanisms. As shown in SI Appendix, Fig. S3, graphenes with HTB concentration of  $\geq 5$  mM are covered by continuous HTB films. Further UPS measurement

shows that pure HTB is characterized by a high work function of 5.3 eV (SI Appendix, Fig. S9A). Therefore, the formation of high work-function coating dominates the surface property of graphene films doped with HTB.

**Mechanisms of Improved Electrical and Optical Performances.** To understand the mechanism of strong and stable doping of HTB on graphene, we performed X-ray photoelectron spectroscopy (XPS) analysis and density functional theory (DFT) calculation. As shown in SI Appendix, Fig. S9B, the binding energy of both B 1s and F 1s in HTB remains almost unchanged after doping graphene, suggesting that the B-C and C-F bondings in tetrakis(pentafluorophenyl)borate anion ( $\text{TB}^-$ ) are not altered. Because HTB is a powerful proton ( $\text{H}^+$ ) donor, it is reasonable to believe that HTB would deprotonate to p-dope graphene (11). The released  $\text{H}^+$  may accept an electron from graphene to become a free H radical ( $\text{H}^\bullet$ ), which results in the formation of positively charged graphene binded by a  $\text{TB}^-$  anion. The newly formed free-H radicals would further form an adduct with the solvent nitromethane (34) or bind another H radical (35).

We then studied the interaction between the  $\text{TB}^-$  anion and the positively charged graphene by DFT. To simplify the calculation, we consider that the above interaction is equivalent to the interaction between the TB radical ( $\text{TB}^\bullet$ ) and neutral graphene. After full relaxation, the Fermi level of graphene downshifts by  $\sim 0.78$  eV from the Dirac point (Fig. 3A), indicating the strong hole doping of graphene and large increase in its work function. Integral density of states (DOS) analysis confirms that one electron is donated from graphene to the  $\text{TB}^\bullet$  to form a  $\text{TB}^-$  anion. Note that the B-C and C-F bond characteristics in the  $\text{TB}^\bullet$  on graphene is basically identical to those in HTB (SI Appendix, Table S2), which confirms the validity of the equivalent calculation. Furthermore, we compared the adsorption energy

( $E_{ad}$ ) of TB<sup>•</sup> on graphene with that of one representative dopant TFSA (*SI Appendix, Fig. S10*). The obtained  $E_{ad}$  of TB<sup>•</sup> with two ethers on graphene is as high as 3.377 eV, which is significantly larger than that (2.397 eV) of TFSA<sup>•</sup> on graphene. It is well known that TFSA shows good ambient doping stability among the reported SCT dopants (28). The larger  $E_{ad}$  explains the higher doping stability of HTB.

Regarding the improved visible transmittance, the relatively small  $E_F$  ( $\leq 0.7$  eV) of HTB-coated graphene suggests that this improvement should not be attributed to the reduced interband absorption caused by doping, which requires a much larger  $E_F$  ( $\sim 1.55$  eV) for the entire visible range ( $\hbar\omega = 1.6\text{--}3.1$  eV) according to  $\hbar\omega < 2E_F$  (36). This  $E_F$  corresponds to an extremely high carrier concentration of  $\sim 6 \times 10^{14}$  cm<sup>-2</sup> (9), which is also significantly higher than our case (hole concentration  $\leq 3.4 \times 10^{13}$  cm<sup>-2</sup>). Instead, we found that the optical reflectance of graphene over the visible range is gradually reduced with the increase of HTB concentration, yielding a notable reduction in absolute value (e.g., 3% at  $\lambda = 550$  nm) for the 20-mM sample (Fig. 3B). *SI Appendix, Figs. S3 and S11* show that thin films of HTB are gradually formed on the surface of graphene with increasing the concentration from 1 to 20 mM, the average thickness of which increases from 3.1 to 11.6 nm. These HTB films show relatively low refractive index ( $n = 1.5$  at  $\lambda = 550$  nm, Fig. 3C) and small transmittance loss (0.1–1.7% at  $\lambda = 550$  nm, Fig. 3D). According to the principle of antireflection film, the presence of low-index HTB film on high-index graphene ( $n = \sim 2.6$  at  $\lambda = 550$  nm) (37) and PET substrate ( $n = \sim 1.65$  at  $\lambda = 550$  nm) (38) enables the destructive interference of reflected light from the graphene/PET film (Fig. 3E). This effect causes the thickness-dependent sinusoidal variation in reflectance, in which the minimum occurs at certain thicknesses ( $d = m\lambda/4n$ ,  $m = 1, 3, 5, \dots$ ) (39). In our case, the minimum HTB thickness to

achieve the reflectance minimum is 95.4 nm at  $\lambda = 550$  nm, below which the reflectance gradually decreases with the thickness of HTB. Considering that HTB coating not only reduces reflectance but also leads to transmittance loss, we first calculated the transmittance increase on the basis of antireflection effect and then subtracted the transmittance loss caused by HTB coating (Fig. 3F). The calculated results agree well with the experimental results, indicating that the improved optical transmittance of HTB-doped graphene is primarily attributed to the antireflection effect of HTB coating (thickness  $\leq 11.6$  nm).

**High-Performance Flexible OLEDs.** We further demonstrate that the use of HTB-coated monolayer graphene film as anode enables high-efficiency flexible phosphorescent green OLEDs. The typical efficiencies of OLEDs are defined as follows: current efficiency  $CE = L/J$  and power efficiency  $PE = f_D \cdot \pi \cdot L/J \cdot V$ , where  $L$ ,  $J$ ,  $V$ , and  $f_D$  refer to luminance intensity, current density, voltage, and a factor relating to the light angular distribution, respectively; external quantum efficiency (EQE) is the product of internal quantum efficiency (IQE) and light outcoupling efficiency (40). CE can be improved by increasing the luminance intensity at a given current intensity while PE will be further enhanced by lowering the operating voltage. For a given IQE, EQE can be significantly improved by increasing the light-coupling efficiency (and thus the increased luminance intensity). Regarding a graphene transparent electrode, the appropriate work function promotes charge injection to improve luminance intensity while the low  $R_s$  allows a lower operating voltage. Moreover, the high transparency is also important for increasing luminance intensity by improving the light outcoupling efficiency. Therefore, the HTB-coated monolayer graphene is a promising anode material for high-efficiency OLEDs in terms of its higher work function ( $\sim 5.3$  eV) and optical transmittance ( $\sim 98\%$ ).

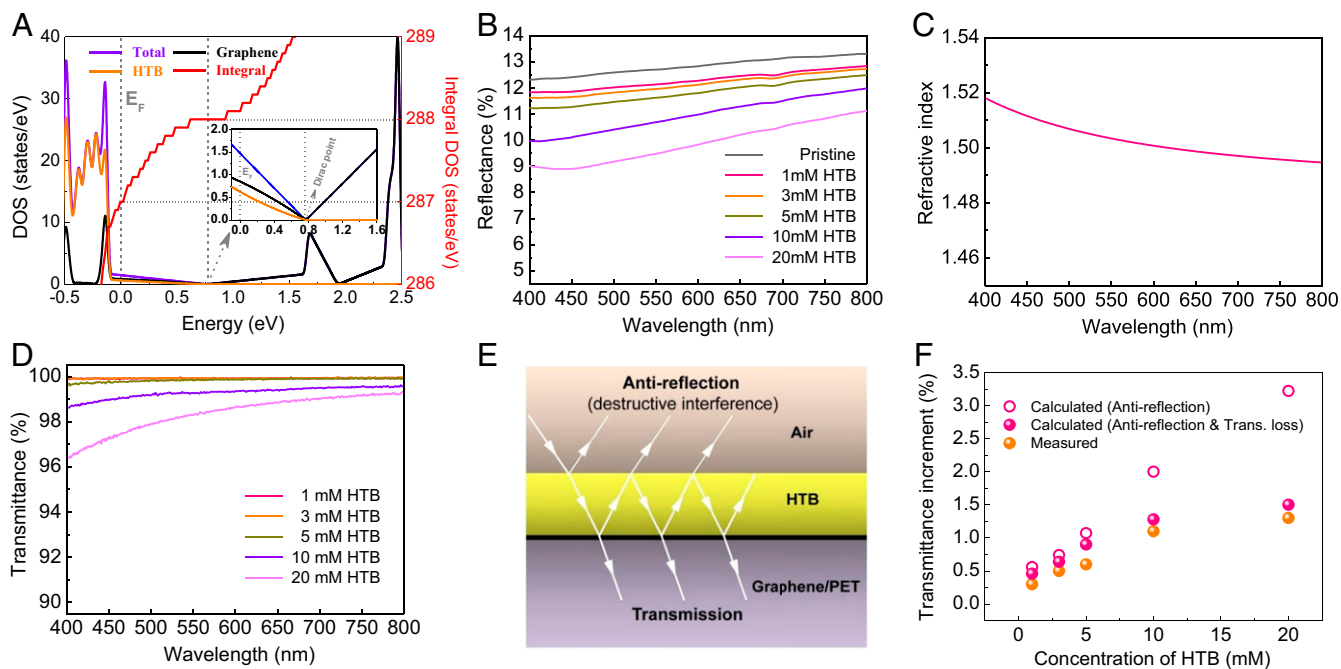


**Fig. 3.** Mechanisms of improved electrical conductance and optical transmittance by HTB coating. (A) DOS of a TB<sup>•</sup> radical on graphene surface calculated by using DFT. (Inset) Enlarged DOS plot near the Dirac point of graphene. The two ether molecules were included as an essential component of HTB in the calculation. (B) Optical reflectance spectra of graphene/PET films coated with different concentrations of HTB. (C) Refractive index of HTB film as a function of wavelength. (D) Optical transmittance spectra of HTB films formed with different concentrations (excluding the quartz substrate). (E) Schematic antireflection effect of HTB coating on graphene/PET film. (F) Comparison of measured transmittance increase with that calculated on the basis of antireflection effect as a function of HTB concentration. Considering the transmittance loss caused by HTB coating as shown in D, we subtracted such loss from the calculated transmittance increase to evaluate the actual transmittance increase caused by HTB coating.

Fig. 4A shows the schematic structure of our HTB-coated monolayer graphene-based OLEDs. We first evaluated the effect of HTB concentration on the device performances and found that the 5 mM HTB-coated sample enables the optimum efficiencies (SI Appendix, Fig. S12). We then compared its performances with those made by using pristine graphene and ITO anodes. Although both graphene-based devices show a similar turn-on voltage of  $\sim 2.5$  V, the use of HTB-coated graphene anode reduces the operating voltage from 4.7 to 4.3 V at the luminance intensity of  $1,000 \text{ cd m}^{-2}$  (SI Appendix, Fig. S13A), suggesting that the hole injection is promoted (11, 12). We note that the  $R_s$  of pristine graphene was slightly reduced to  $494 \pm 27 \Omega/\square$  by the p-doping of deposited  $\text{MoO}_3$  layer, but it is still higher than that of HTB-coated graphene with  $\text{MoO}_3$  layer ( $168 \pm 13 \Omega/\square$ ). Therefore, the improved hole injection is attributed to the higher work function (5.3 eV vs. 4.6 eV) and lower  $R_s$  of the latter. This favorable effect enables significant improvement in the overall performances of OLED. As shown in Fig. 4, the HTB-coated monolayer graphene-based OLEDs show maximum CE, PE, and EQE of  $111.4 \text{ cd A}^{-1}$ ,  $124.9 \text{ lm W}^{-1}$ , and 29.7%, respectively. These values are increased by 33, 56, and 33% compared to those of the pristine graphene-based OLED. We also note the device with HTB-coated graphene shows lower current density and higher operating voltage than the ITO device at voltages above 4 V due to its much higher  $R_s$  of electrode ( $168 \pm 13 \Omega/\square$  vs.  $8 \Omega/\square$ ). However, its maximum CE, PE, and EQE are still significantly higher than those of ITO device by 31, 43, and 31%, respectively. Further comparison with the state-of-the-art flexible OLEDs demonstrates that our device shows record-high efficiencies not only among devices with heavily doped monolayer and few-layer graphene anodes, but also among those with other high-performance flexible anodes (Fig. 4E and F) (5, 11, 12, 14, 19, 41–48). The identical electroluminescence spectra of green emission obtained at different voltages indicate the high stability of the devices (SI Appendix, Fig. S13B), which benefits from the excellent stability of HTB doping.

Moreover, HTB coating improves the operational stability of OLEDs with graphene anodes even under ambient condition (SI Appendix, Fig. S13C). We further evaluated the bending stability of graphene-based OLEDs by examining the electroluminescence intensity decay over bending cycles under ambient condition. As shown in SI Appendix, Fig. S13D, our OLEDs demonstrate good stability over repeated bending. The device with the HTB-coated graphene anode shows a moderate luminance decay of 19% after 1,000 cycles. This performance is comparable to that (21% decay) of device with the pristine graphene anode. These results indicate that the bending stability is well retained by using the HTB-coated anode. We expect that both the operational stability and bending stability can be significantly improved if the devices are encapsulated to minimize the detrimental effects of oxygen and moisture in air. Fig. 4F, Inset and Movie S1 show a monolithic flexible green OLED with a lighting area of 1 inch in diagonal size. Note that the strong luminescence is uniform over the whole lighting area and it remains stable over repeated bending, which further confirms the high bending stability shown above. It demonstrates that HTB-coated graphene is a promising anode material for large-area flexible OLEDs.

To gain further insight into the effect of HTB coating on improving device performances, we first compared the hole injection of the hole-only devices that were fabricated with HTB-coated graphene and those doped with the three typical p-dopants ( $\text{HNO}_3$ , OA, and TFSA). As shown in SI Appendix, Fig. S13E and F, the HTB coating allows higher current density than  $\text{HNO}_3$ , OA, and TFSA doping at a given voltage, with  $\sim 24$  and  $\sim 50\%$  increase at 5 and 8 V, respectively. Such large improvement clearly reveals that the HTB coating enables more efficient hole injection into the hole transportation layer. Considering that all of the four anodes show similar  $R_s$  (Fig. 2B), the superior hole injection of

HTB-doped graphene anode is mainly attributed to its higher work function (5.3 eV) than the other three samples (5.0–5.1 eV, SI Appendix, Fig. S9A) (11, 12). Note that the OLED with pristine monolayer graphene anode (transparency of 97%) shows efficiencies comparable to those of device with ITO anode (lower transparency of  $\sim 88\%$ ) although the graphene anode shows much higher  $R_s$  and lower work function ( $494 \pm 27 \Omega/\square$ , 4.6 eV) than the ITO anode ( $8 \Omega/\square$ , 5.1 eV). This result suggests the substantial contribution of high transparency of graphene anode in boosting the device efficiency by improving the light outcoupling efficiency (14). Therefore, the combination of higher transparency and work function is responsible for higher efficiencies enabled by HTB-coated graphene anode as compared to the ITO device. Currently, most studies focus on improving the electrical conductance of graphene electrodes to improve the device efficiencies of OLED, typically by using doped few-layer graphene. However, the resulting devices show inferior efficiencies to our device with monolayer graphene even though their electrodes show significantly higher conductance (e.g., lower  $R_s$  of  $54 \Omega/\square$ ) (19), as shown in Fig. 4E and F. This comparison further highlights the significance of high transparency of graphene anode in achieving high-efficiency OLEDs. Retaining such high transparency and further lowering the sheet resistance of graphene anode would be essential to unlock the potential of graphene OLEDs, especially for the large-area devices.

## Conclusions

In summary, we have described a straightforward pathway to break previous limit in graphene FTEs and yielded an unprecedented FoM that rivals the best commercial ITO electrode. Using the tailored monolayer graphene anode, we further demonstrate high-performance flexible green OLEDs with the maximum efficiencies outperforming all comparable flexible OLEDs and surpassing that with standard rigid ITO anode. We expect that a versatile strategy would be established by exploring the broad choices of organic and inorganic coatings that are effective for other carbon-based or two-dimensional FTEs with diverse functionalities. The resulting FTEs will boost the development of next-generation flexible optoelectronics beyond the dominant rigid platforms.

## Materials and Methods

**CVD Growth and Transfer of Graphene.** Monolayer polycrystalline and single-crystal graphene films were synthesized by CVD on copper foil. For the growth of polycrystalline graphene, a commercial copper foil (99.9%, 25- $\mu\text{m}$  thick, Aluminum Corporation of China) was used as received. The copper foil was first annealed at  $1,000^\circ\text{C}$  under a 5-sccm hydrogen flow and then exposed to the mixture of hydrogen (5 sccm) and methane (60 sccm) at a total pressure of 100 Pa for 30 min to grow graphene, followed by slow cooling to room temperature. Single-crystal graphene film was grown on a single-crystal Cu(111) foil, the details of which can be found in ref. (49).

After growth, graphene was transferred by using the poly(methyl methacrylate) (PMMA) method or the rosin method (5). The PMMA transfer method was used for most structure and property characterizations. Specifically, the solution of PMMA was first spin-coated on the graphene/Cu foil and cured. After removing the Cu foil by chemical etching or bubbling delamination, the PMMA/graphene film was transferred to the PET or  $\text{SiO}_2/\text{Si}$  substrate, followed by acetone immersion to remove PMMA. The films transferred on PET were used for optical transmittance, sheet resistance, and Hall measurements, while those on  $\text{SiO}_2/\text{Si}$  substrate were used for Raman, UPS, and FET measurements. The rosin transfer method was used for preparing the atomic force microscope (AFM) samples and OLED electrodes since it can achieve clean graphene.

**HTB Coating and Chemical Doping of Graphene.** HTB was synthesized following the reported procedures (10). Triethyloxonium hexachloroantimonate (OA, Sigma-Aldrich), gold chloride ( $\text{AuCl}_3$ , Sigma-Aldrich), Bis(trifluoromethane) sulfonimide (TFSA, Sigma-Aldrich), and nitric acid ( $\text{HNO}_3$ , Sinoreagent) were used as received. HTB coating and chemical doping of graphene with OA,  $\text{AuCl}_3$ , and TFSA was performed by dip-coating the samples in their

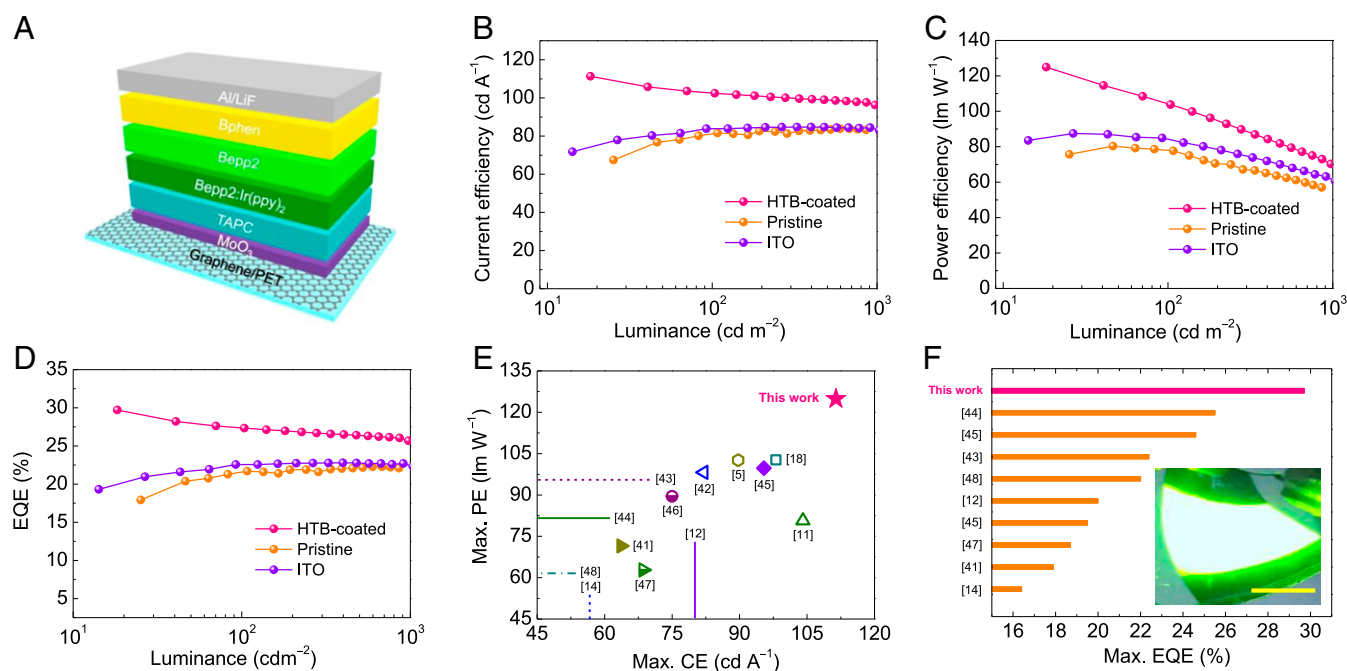


**Fig. 4.** Structure and performances of flexible green OLEDs with HTB-coated graphene anode. (A) Schematic device structure of OLED. (B) CE, (C) PE, and (D) EQE versus luminance characteristics of OLEDs with pristine monolayer graphene, HTB-coated monolayer graphene and ITO films as anodes. (E) Maximum PE, CE and (F) maximum EQE comparison of flexible green OLEDs using HTB-coated monolayer graphene anode with other state-of-the-art flexible green OLEDs (standard, single) using different anodes without light-extraction structures (e.g., lenses, scattering, or cavity resonance enhancement design). The open (dashed) and filled (solid) symbols (lines) in E denote the few-layer and monolayer graphene anode, respectively. (F, *Inset*) A 1-inch monolithic flexible green OLED with the HTB-coated graphene anode, showing strong, uniform luminance and good flexibility. (Scale bar, 10 mm.)

nitromethane solutions while  $\text{HNO}_3$  doping was performed by exposing the graphene film to the vapor of  $\text{HNO}_3$ , which were then dried by nitrogen flow.

**Structure and Property Characterization.** Raman spectra were recorded under the excitation of a 532-nm laser by using a confocal Raman spectrometer (Jobin Yvon Lab RAM HR800). The carrier concentration and mobility of graphene films on PET were measured by using a Hall-effect measurement meter (Ecopia, HMS-5000), and the size of graphene films was  $10 \times 10 \text{ mm}^2$ . The sheet resistance was measured by using the four-point probe method (4Probes Tech Corp.). The transmittance spectra of graphene films were collected by using an UV-vis-near infrared ray spectrometer (Varian Cary 5000) with the blank PET substrate as the reference. The surface morphology was characterized by using an AFM (Bruker, Multimode 8). The average thickness and refractive index of HTB film were measured by using an ellipsometer (J.A. Woollam Co., Inc., RC2-X1). XPS and UPS measurements were performed by using an ESCALAB 250 instrument with Al  $K_{\alpha}$  and He I (21.22 eV) radiation sources, respectively. Work function was calculated by using the equation  $\phi = h\nu + E_{\text{cutoff}} - E_{\text{Fermi}}$ .

For FET measurements, graphene film was first transferred onto the  $\text{SiO}_2$  (100 nm)/Si substrate with the prepatterned Ti/Au as the source/drain electrodes and the predeposited Au film as the bottom gate, and then patterned by using standard photolithography and oxygen plasma etching to fabricate FET with a channel size of  $5 \mu\text{m} \times 100 \mu\text{m}$ . The electrical measurements of the devices were performed by using a semiconductor analyzer (Agilent, B1500A) at ambient condition.

**DFT Calculations.** DFT calculations were performed by using the Vienna Ab initio Simulation Package with the projector augmented wave (PAW) method. The Perdew–Burke–Ernzerhof (PBE) functional for the exchange–correlation term was used for all calculations. The PAW method was used at a plane-wave cutoff of 400 eV to describe the electron–ion interaction. Spin-polarized calculations were performed for systems with an odd number of electrons. A  $5 \times 5$  graphene sheet with 50 carbon atoms was used to study TFSA doping, while a  $6 \times 6$  graphene sheet with 72 carbon atoms was used to study HTB doping. The distance between two periodic graphene images along z direction was set to be 30 Å. A Monkhorst-Pack ( $3 \times 3 \times 1$ ) k-point mesh was used to sample the Brillouin zone for all calculations. For the

geometry relaxations and energy calculations, van der Waals interactions were incorporated by the optB88 exchange functional to accurately evaluate the interactions between adsorbate and graphene. All atoms were fully relaxed within the fixed graphene supercell until the residual force per atom decreases to below  $0.01 \text{ eV \AA}^{-1}$ .

**Fabrication and Measurements of OLEDs.** Pristine and HTB-coated polycrystalline monolayer graphene films on PET were directly used as the anode. To minimize the detrimental effect of particle residue, the rosin-based clean transfer method (5) was used to transfer graphene onto PET substrate instead of the typical PMMA method. ITO/glass anodes were sequentially cleaned by acetone, alcohol, and deionized water, followed by UV/ozone treatment prior to use. Then, the anodes were loaded into a home-made thermal evaporation system to deposit a  $\text{MoO}_3$  hole injection layer, organic films, and a cathode. The phosphorescent green OLEDs consist of graphene/PET (ITO/glass) anodes, a 10 nm  $\text{MoO}_3$  hole injection layer, organic films, and a cathode. The phosphorescent green OLEDs consist of graphene/PET (ITO/glass) anodes, a 10 nm  $\text{MoO}_3$  hole injection layer, a 60 nm di-(4-(N,N-ditolyl-amino)-phenyl)cyclohexane (TAPC) hole-transportation layer, a 10 nm emitting layer of bis(2-phenylpyridine)(acetylacetonate) iridium(III) ( $\text{Ir(ppy)}_2(\text{acac})$ ) doped into Bis(2-(2-hydroxyphenyl)-pyridine)beryllium (Bepp2), a 10 nm Bepp2 exciton blocking layer, a 50 nm bathophenanthroline (Bphen) electron-transporting layer and a 1 nm LiF/100 nm Al cathode. The typical active area for performance measurements was  $4 \times 4 \text{ mm}^2$  and a large-size device with an active area of  $20 \times 16 \text{ mm}^2$  was fabricated for demonstration. The hole-only devices: PET/monolayer graphene/ $\text{MoO}_3$  (10 nm)/TAPC (30 nm)/Bepp2: $\text{Ir(ppy)}_2(\text{acac})$  (10%, 10 nm)/TAPC (30 nm)/ $\text{MoO}_3$  (10 nm)/Al (100 nm). Current–brightness–voltage characteristics of the unencapsulated OLEDs were measured by Keithley source measurement units (Keithley 2400 and Keithley 2000) with a calibrated silicon photodiode under ambient condition.

**Data Availability.** All study data are included in the article and *SI Appendix*.

**ACKNOWLEDGMENTS.** We sincerely thank Prof. Libo Gao, Dr. Jianhang Qiu, Dr. Yun Sun, Mr. Guowen Yuan, Mr. Hang Zheng, and Mr. Zhigang Lu for their experimental assistance, and Dr. Songfeng Pei and Dr. Chuan Xu for their helpful discussions. This work was supported by the Ministry of Science and Technology of China (Grant 2016YFA0200101 and 2016YFB04001104), National Natural Science Foundation of China (Grants 51325205, 51290273, 51521091, 51272256, 61422406, 61574143, and 51861135201), Chinese

Academy of Sciences (Grants ZDBS-LY-JSC027, XDB30000000, KGZD-EW-303-1, KGZD-EW-303-3, and KGZD-EW-T06), the Liaoning Revitalization Talents Program (Grant XLYC1808013), and the Program for Guangdong Introducing

Innovative and Entrepreneurial Teams and the Development and Reform Commission of Shenzhen Municipality for the development of the "Low-Dimensional Materials and Devices" discipline.

1. Y. Ma, L. Zhi, Graphene-based transparent conductive films: Material systems, preparation and applications. *Small Methods* **3**, 1800199 (2019).
2. K. Ellmer, Past achievements and future challenges in the development of optically transparent electrodes. *Nat. Photonics* **6**, 809–817 (2012).
3. W. W. Cai, Y. W. Zhu, X. S. Li, R. D. Piner, R. S. Ruoff, Large area few-layer graphene/graphite films as transparent thin conducting electrodes. *Appl. Phys. Lett.* **95**, 123115 (2009).
4. S. Bae et al., Roll-to-roll production of 30-inch graphene films for transparent electrodes. *Nat. Nanotechnol.* **5**, 574–578 (2010).
5. Z. Zhang et al., Rosin-enabled ultraclean and damage-free transfer of graphene for large-area flexible organic light-emitting diodes. *Nat. Commun.* **8**, 14560 (2017).
6. J. H. Min, W. L. Jeong, H. M. Kwak, D. S. Lee, High-performance metal mesh/graphene hybrid films using prime-location and metal-doped graphene. *Sci. Rep.* **7**, 10225 (2017).
7. E. H. Cho et al., A graphene mesh as a hybrid electrode for foldable devices. *Nanoscale* **10**, 628–638 (2018).
8. X. Zhang, Z. Shao, X. Zhang, Y. He, J. Jie, Surface charge transfer doping of low-dimensional nanostructures toward high-performance nanodevices. *Adv. Mater.* **28**, 10409–10442 (2016).
9. W. Bao et al., Approaching the limits of transparency and conductivity in graphitic materials through lithium intercalation. *Nat. Commun.* **5**, 4224 (2014).
10. I. Hatay et al., Oxygen reduction catalyzed by a fluorinated tetraphenylporphyrin free base at liquid/liquid interfaces. *J. Am. Chem. Soc.* **132**, 13733–13741 (2010).
11. T. H. Han et al., Versatile p-type chemical doping to achieve ideal flexible graphene electrodes. *Angew. Chem. Int. Ed. Engl.* **55**, 6197–6201 (2016).
12. N. Li et al., Efficient and bright organic light-emitting diodes on single-layer graphene electrodes. *Nat. Commun.* **4**, 2294 (2013).
13. Y. M. Seo et al., 2D doping layer for flexible transparent conducting graphene electrodes with low sheet resistance and high stability. *Adv. Electron. Mater.* **4**, 1700622 (2018).
14. I. J. Park et al., Flexible and transparent graphene electrode architecture with selective defect decoration for organic light-emitting diodes. *Adv. Funct. Mater.* **28**, 1704435 (2018).
15. J. E. Lee, G. Ahn, J. Shim, Y. S. Lee, S. Ryu, Optical separation of mechanical strain from charge doping in graphene. *Nat. Commun.* **3**, 1024 (2012).
16. C. Neumann et al., Raman spectroscopy as probe of nanometre-scale strain variations in graphene. *Nat. Commun.* **6**, 8429 (2015).
17. M. Kim et al., Highly stable and effective doping of graphene by selective atomic layer deposition of ruthenium. *ACS Appl. Mater. Interfaces* **9**, 701–709 (2017).
18. F. Güneş et al., Layer-by-layer doping of few-layer graphene film. *ACS Nano* **4**, 4595–4600 (2010).
19. T. H. Han et al., Extremely efficient flexible organic light-emitting diodes with modified graphene anode. *Nat. Photonics* **6**, 105–110 (2012).
20. S. J. Kim et al., Simultaneous etching and doping by Cu-stabilizing agent for high-performance graphene-based transparent electrodes. *Chem. Mater.* **26**, 2332–2336 (2014).
21. B. H. Lee et al., Graphene-conducting polymer hybrid transparent electrodes for efficient organic optoelectronic devices. *Adv. Funct. Mater.* **24**, 1847–1856 (2014).
22. V. P. Pham, K. N. Kim, M. H. Jeon, K. S. Kim, G. Y. Yeom, Cyclic chlorine trap-doping for transparent, conductive, thermally stable and damage-free graphene. *Nanoscale* **6**, 15301–15308 (2014).
23. J. Kang et al., High-performance graphene-based transparent flexible heaters. *Nano Lett.* **11**, 5154–5158 (2011).
24. S. H. Bae et al., Graphene-P(VDF-TrFE) multilayer film for flexible applications. *ACS Nano* **7**, 3130–3138 (2013).
25. D. Kim, D. Lee, Y. Lee, D. Y. Jeon, Work-function engineering of graphene anode by bis(trifluoromethanesulfonyl)amide doping for efficient polymer light-emitting diodes. *Adv. Funct. Mater.* **23**, 5049–5055 (2013).
26. T. Kobayashi et al., Production of a 100-m-long high-quality graphene transparent conductive film by roll-to-roll chemical vapor deposition and transfer process. *Appl. Phys. Lett.* **102**, 023112 (2013).
27. L. P. Ma et al., UV-epoxy-enabled simultaneous intact transfer and highly efficient doping for roll-to-roll production of high-performance graphene films. *ACS Appl. Mater. Interfaces* **10**, 40756–40763 (2018).
28. J. H. Heo et al., Super-flexible bis(trifluoromethanesulfonyl)-amide doped graphene transparent conductive electrodes for photo-stable perovskite solar cells. *J. Mater. Chem. A* **6**, 8251–8258 (2018).
29. S. J. Kwon et al., Extremely stable graphene electrodes doped with macromolecular acid. *Nat. Commun.* **9**, 2037 (2018).
30. K. C. Kwon, K. S. Choi, S. Y. Kim, Increased work function in few-layer graphene sheets via metal chloride doping. *Adv. Funct. Mater.* **22**, 4724–4731 (2012).
31. Y. Shi et al., Work function engineering of graphene electrode via chemical doping. *ACS Nano* **4**, 2689–2694 (2010).
32. K. Yokota, K. Takai, T. Enoki, Carrier control of graphene driven by the proximity effect of functionalized self-assembled monolayers. *Nano Lett.* **11**, 3669–3675 (2011).
33. K. S. Novoselov et al., Two-dimensional gas of massless Dirac fermions in graphene. *Nature* **438**, 197–200 (2005).
34. M. Polasek, F. Turecek, Direct observation of hydrogen atom adducts to nitromethane and methyl nitrite. A variable-time neutralization-reionization mass spectrometric and ab initio/RRKM study. *J. Phys. Chem. A* **103**, 9241–9251 (1999).
35. M. Lozada-Hidalgo et al., Giant photoeffect in proton transport through graphene membranes. *Nat. Nanotechnol.* **13**, 300–303 (2018).
36. A. C. Crowther, A. Ghassaei, N. Jung, L. E. Brus, Strong charge-transfer doping of 1 to 10 layer graphene by NO<sub>2</sub>. *ACS Nano* **6**, 1865–1875 (2012).
37. E. Ochoa-Martínez et al., Determination of a refractive index and an extinction coefficient of standard production of CVD-graphene. *Nanoscale* **7**, 1491–1500 (2015).
38. J. C. Martínez-Anton, E. Bernabeu, Spectrogoniometry and the wanted method for thickness and refractive index determination. *Thin Solid Films* **313**, 85–89 (1998).
39. S. O. Kasap, *Optoelectronics & Photonics: Principles & Practices*, (Pearson, ed. 2, 2013).
40. Z. B. Wu, D. G. Ma, Recent advances in white organic light-emitting diodes. *Mater. Sci. Eng. Rep.* **107**, 1–42 (2016).
41. C. H. Chang, J. L. Huang, S. W. Wu, Mo-doped GZO films used as anodes or cathodes for highly efficient flexible blue, green and red phosphorescent organic light-emitting diodes. *J. Mater. Chem. C* **3**, 12048–12055 (2015).
42. S. Jia et al., Graphene oxide/graphene vertical heterostructure electrodes for highly efficient and flexible organic light emitting diodes. *Nanoscale* **8**, 10714–10723 (2016).
43. J. Lee et al., Synergetic electrode architecture for efficient graphene-based flexible organic light-emitting diodes. *Nat. Commun.* **7**, 11791 (2016).
44. Q. Li et al., Nickelocene-precursor-facilitated fast growth of graphene/h-BN vertical heterostructures and its applications in OLEDs. *Adv. Mater.* **29**, 1701325 (2017).
45. T. L. Wu et al., High-performance organic light-emitting diode with substitutionally boron-doped graphene anode. *ACS Appl. Mater. Interfaces* **9**, 14998–15004 (2017).
46. S. Jiang et al., Ultrahigh-performance transparent conductive films of carbon-welded isolated single-wall carbon nanotubes. *Sci. Adv.* **4**, eaap9264 (2018).
47. J. Lee et al., A dual-scale metal nanowire network transparent conductor for highly efficient and flexible organic light emitting diodes. *Nanoscale* **9**, 1978–1985 (2017).
48. Y. S. Oh et al., Temperature-controlled direct imprinting of Ag ionic ink: Flexible metal grid transparent conductors with enhanced electromechanical durability. *Sci. Rep.* **7**, 11220 (2017).
49. X. Z. Xu et al., Ultrafast epitaxial growth of metre-sized single-crystal graphene on industrial Cu foil. *Sci. Bull.* **62**, 1074–1080 (2017).